

Implementable Efficient Time and Energy Consumption Trajectories Design For an Autonomous Underwater Vehicle

Monique Chyba, Thomas Haberkorn, University of Hawaii Manoa, Hawaii/USA,
mchyba@math.hawaii.edu

Ryan N. Smith, University of Hawaii Manoa, Hawaii/USA, ryan@math.hawaii.edu

Song K. Choi, University of Hawaii Manoa, Hawaii/USA

Abstract

In this paper we consider the implementation of time and energy efficient trajectories onto a test-bed autonomous underwater vehicle. The trajectories are loosely connected to the results of the application of the maximum principle to the controlled mechanical system. We use a numerical algorithm to compute efficient trajectories designed using geometric control theory to optimize a given cost function. Experimental results are shown for the time minimization problem.

1 Introduction

The oceans cover over 75% of the earth's surface and are currently exploited for energy, recreation, transportation, food and much more. However, almost 95% of this vast resource is unexplored. What other resources lie beneath the surface of the water? What else does the ocean have to offer? The answer to these questions among many others can only be answered through extensive ocean research and exploration. Today's maritime industries and research communities employ the use of underwater vehicles as a method to help discover the secrets of the abyss. Whether it is searching for oil deposits in the Gulf of Mexico, monitoring a coral reef in Papahānaumokuākea Marine National Monument (formerly the Northwestern Hawaiian Islands Marine National Monument), or just gathering data in Monterey Bay, underwater vehicles play a large part in understanding the oceans. Due to the extensive role that these vehicles play, their autonomy has become a large research interest. Much research has gone into making autonomous vehicles that travel underwater and perform a multitude of tasks far surpassing the abilities of human divers and small human-driven submarines. This extension of tasks also reduces the risk to humans while still gaining information about the vast ocean. This has motivated the research and development of AUV's and their control systems to have the ability to take over more responsibilities in ocean research. As we give a vehicle more responsibilities, assuming all else is constant, it will require an increase in efficiency. To do this we search for optimal trajectories which minimize some cost, such as time or energy. This is the basis for optimal control theory. We all know of many success stories in the AUV community; Kongsberg's HUGIN and WHOI's REMUS are well known. But, even with such successes in AUV control, optimal control is still a very underdeveloped area. Adaptive control research has contributed to cost minimization problems, but vehicle design has been the driving force for advancement in optimal control research. We look to advance the development of optimal control theory by expanding the motions along which AUV's travel. Traditionally, AUV's have taken the role of performing the long data gathering mission in the open ocean with little to no interaction with their surroundings *MacIver et al. (2004)*. The AUV is used to find the shipwreck, and the remotely operated vehicle (ROV) handles the up close exploration. AUV mission profiles of this sort are best suited through the use of a torpedo shaped AUV, *Bertram and Alvarez (2006)*, such as WHOI's REMUS and MIT's Odyssey, since straight lines and minimal (0° - 30°) angular displacements are all that are necessary to perform the transects and grid lines for these applications. However, the torpedo shape AUV lacks the ability to perform low-speed maneuvers in cluttered environments, such as autonomous exploration close to the seabed and around obstacles *MacIver et al. (2004)*, *Molnar et al. (2005)*. To this end, we approach the problem from a geometric control viewpoint and study optimal trajectories for vehicles with unconstrained movement in six degrees of freedom. From a practical point of view, this increases the difficulty of the control problem. However, without any movement constraints, the tools of geometric control theory are able to exploit the inherent nonlinear structure of the mechanical system and increase the size of the control domain. This

results in a greater understanding of the geometric properties of the AUV as a mechanical system. Expanding our knowledge based on theory alone is insufficient, especially in such a practical field as AUV control. In parallel to the theoretical study, we conduct weekly experiments on a test-bed AUV in order to validate our algorithms. This gives us a benchmark in both theory and application as to the limitations of one on the other. With all of these tools in hand, we are well suited to bridge the gap between geometric control theory and optimal control application onto AUV's.

2 Equations of Motion

The equations of motion for a submerged rigid body have been extensively studied, *Fossen (1996)*. We will not repeat the derivation of these equations but rather add some comments which we consider very important, and which are usually omitted from AUV literature.

First we precisely define the configuration space of a rigid body. We identify the position and the orientation of a rigid body with an element of the matrix group of rigid displacements $SE(3)$: (b, R) , where $b = (b_1, b_2, b_3)^t \in \mathbb{R}^3$ denotes the position vector of the body and $R \in SO(3)$ is a rotation matrix describing the orientation of the body. The translational and angular velocities in the body-fixed frame are denoted by $v = (v_1, v_2, v_3)^t$ and $\Omega = (\Omega_1, \Omega_2, \Omega_3)^t$ respectively. It follows that the kinematic equations of a rigid body are given by: $\dot{b} = Rv$, $\dot{R} = R\hat{\Omega}$ where the operator $\hat{\cdot} : \mathbb{R}^3 \rightarrow so(3)$ is defined by $\hat{y}z = y \times z$; $so(3)$ being the space of skew-symmetric matrices. Notice that the linear space of the body-fixed velocities is the Lie algebra $\mathfrak{se}(3)$. We assume for the rest of the paper that the origin of the body-fixed frame is the center of gravity C_G . Moreover, we assume the body to have three planes of symmetry with body axes which coincide with the principal axes of inertia. The kinetic energy of the rigid body is then given by $T_{body} = \frac{1}{2}\xi^t \mathbb{I} \xi$ where \mathbb{I} is the inertia matrix and $\xi = (v, \Omega)$.

We now assume that the body is immersed in a real fluid. By real fluid we mean a viscous ideal fluid. Here a real fluid is assumed to be irrotational, but from a practical point of view a viscous fluid is rotational. Our assumptions on the vehicle imply that the body inertia, the added mass and the moment of inertia matrices are diagonal, and the added cross-terms are zero. It follows that the total kinetic energy of our rigid body in an unbounded real fluid is given by $T = \frac{1}{2}(v^t(mI_3 + M_f)v + \Omega^t(J_b + J_f)\Omega)$ where m is the mass of the rigid body, I_3 is the 3×3 -identity matrix and J_b is the body inertia matrix. Moreover, M_f, J_f are respectively referred to as the added mass and the added moments of inertia. These coefficients depend on the density of the fluid. In the sequel we will use $M = mI_3 + M_f$ and $J = J_b + J_f$. The Coriolis and centripetal effects can be expressed in terms of ∇ ; the Levi-Civita affine-connection for the Riemannian metric induced by the kinetic energy T . Explicitly, if $\gamma(t) = (b(t), R(t))$ is a curve in $SE(3)$, and $\gamma'(t) = (v(t), \Omega(t))$ is its pseudo-velocity, then

$$\nabla_{\gamma'}\gamma' = \begin{pmatrix} \dot{v} + M^{-1}(\Omega \times Mv) \\ \dot{\Omega} + J^{-1}(\Omega \times J\Omega + v \times Mv) \end{pmatrix} \quad (1)$$

. Gravity, buoyancy, drag and lift can be modeled using external forces and torques. The equations of a rigid body submerged in a real fluid can then be modeled using affine differential geometry. They form a first-order affine control system on the tangent bundle $TSE(3)$ that represents the second-order *forced affine-connection control system* on $SE(3)$

$$\nabla_{\gamma'}\gamma' = \begin{pmatrix} M^{-1}(D_v(v)v + R^t \rho g \mathcal{V}k + \varphi_v) \\ J^{-1}(D_\Omega(\Omega)\Omega - r_B \times R^t \rho g \mathcal{V}k + \tau_\Omega) \end{pmatrix} \quad (2)$$

where ∇ is the Levi-Civita affine-connection for the Riemannian metric induced by the kinetic energy T . The matrices $D_v(v), D_\Omega(\Omega)$ represent the drag force and momentum respectively. Finally, we have a restoring force and a restoring moment. The only moment due to the restoring forces is the torque from the buoyancy force $-r_B \times R^t \rho g \mathcal{V}k$ where r_B is the vector from C_G to the center of buoyancy C_B , where ρ is the fluid density, g the acceleration of gravity, \mathcal{V} the volume of fluid displaced by the rigid body and k the unit vector pointing in the direction of gravity. The forces $\varphi_v = (\varphi_{v_1}, \varphi_{v_2}, \varphi_{v_3})^t$ and $\tau_\Omega = (\tau_{\Omega_1}, \tau_{\Omega_2}, \tau_{\Omega_3})^t$

account for the control. In the absence of restoration, drag forces and momentum the equations of motion (2) represent a *left-invariant affine-connection control system* on the Lie group $\mathcal{SE}(3)$.

System (2) is equivalent to

$$M\dot{v} = Mv \times \Omega + D_v(v)v + R^t \rho g \mathcal{V}k + \varphi_v \quad (3)$$

$$J\dot{\Omega} = J\Omega \times \Omega + Mv \times v + D_\Omega(\Omega)\Omega - r_B \times R^t \rho g \mathcal{V}k + \tau_\Omega \quad (4)$$

which are the form of the equations of motion usually encountered in the literature. We refer interested readers to *Leonard (1996,1997)*, *Chyba et al. (2007)* for an in depth treatment of the geometric features of submerged rigid bodies.

For our computations and experiments we make the following assumptions. We assume a drag force $D_v(v)$ and a drag momentum $D_\Omega(\Omega)$, neglecting the off-diagonal terms. The contribution of these forces is usually assumed to be quadratic in the velocities, more precisely we have $D_v^{ii}(v) = C_D \rho A |v_i| |v_i|$ where C_D for a sphere is taken as 1.2 for laminar flows and 0.2 for turbulent flows, ρ is the density of the fluid and A is the projected surface area of the object. Under these assumptions, the drag force and momentum are then non differentiable functions which causes difficulties for theoretical analysis. To overcome this, some people assume the vehicle to move in a single direction, hence $|v_i| |v_i| = v_i^2$. We do not want to make this assumption, because at least rotations are needed in both directions. Based on our test bed vehicle, our computations for the total drag forces for various velocities are approximated well using a cubic function with no quadratic or constant term. To summarize, the contribution to the translational motions is given by $D_v(v) = \text{diag}(D_v^{i1} v_i^3 + D_v^{i2} v_i)$ and to the rotational motions by $D_\Omega(\Omega) = \text{diag}(D_\Omega^{i1} \Omega_i^3 + D_\Omega^{i2} \Omega_i)$ where D_v^{ij}, D_Ω^{ij} are constant coefficients.

In local coordinates, the equations of motion for a submerged rigid body in a real fluid are as follows. We denote by $\eta = (b_1, b_2, b_3, \phi, \theta, \psi)^t$ the position and orientation of the vehicle with respect to the earth-fixed reference frame. The coordinates ϕ, θ, ψ are the Euler angles for the body frame. The coordinates corresponding to translational and rotational velocities in the body frame are $v = (v_1, v_2, v_3)^t$ and $\Omega = (\Omega_1, \Omega_2, \Omega_3)^t$. We have:

$$\dot{b}_1 = v_1 \cos \psi \cos \theta + v_2 R^{12} + v_3 R^{13} \quad (5)$$

$$\dot{b}_2 = v_1 \sin \psi \cos \theta + v_2 R^{22} + v_3 R^{23} \quad (6)$$

$$\dot{b}_3 = -v_1 \sin \theta + v_2 \cos \theta \sin \phi + v_3 \cos \theta \cos \phi \quad (7)$$

$$\dot{\phi} = \Omega_1 + \Omega_2 \sin \phi \tan \theta + \Omega_3 \cos \phi \tan \theta \quad (8)$$

$$\dot{\theta} = \Omega_2 \cos \phi - \Omega_3 \sin \phi \quad (9)$$

$$\dot{\psi} = \frac{\sin \phi}{\cos \theta} \Omega_2 + \frac{\cos \phi}{\cos \theta} \Omega_3 \quad (10)$$

$$\dot{v}_1 = \frac{1}{m_1} [-(m_3)v_3\Omega_2 + (m_2)v_2\Omega_3 + D_v(v_1) - G \sin \theta + \varphi_{v_1}] \quad (11)$$

$$\dot{v}_2 = \frac{1}{m_2} [(m_3)v_3\Omega_1 - (m_1)v_1\Omega_3 + D_v(v_2) + G \cos \theta \sin \phi + \varphi_{v_2}] \quad (12)$$

$$\dot{v}_3 = \frac{1}{m_3} [-(m_2)v_2\Omega_1 + (m_1)v_1\Omega_2 + D_v(v_3) + G \cos \theta \cos \phi + \varphi_{v_3}] \quad (13)$$

$$\begin{aligned} \dot{\Omega}_1 = & \frac{1}{I_{b_1} + J_f^{\Omega_1}} [(I_{b_2} - I_{b_3} + J_f^{\Omega_2} - J_f^{\Omega_3})\Omega_2\Omega_3 + (M_f^{v_2} - M_f^{v_3})v_2v_3 \\ & + D_\Omega(\Omega_1) + \rho g \mathcal{V}(-y_B \cos \theta \cos \phi + z_B \cos \theta \sin \phi) + \tau_{\Omega_1}] \end{aligned} \quad (14)$$

$$\begin{aligned} \dot{\Omega}_2 = & \frac{1}{I_{b_2} + J_f^{\Omega_2}} [(I_{b_3} - I_{b_1} + J_f^{\Omega_3} - J_f^{\Omega_1})\Omega_1\Omega_3 + (M_f^{v_3} - M_f^{v_1})v_1v_3 \\ & + D_\Omega(\Omega_2) + \rho g \mathcal{V}(z_B \sin \theta + x_B \cos \theta \cos \phi) + \tau_{\Omega_2}] \end{aligned} \quad (15)$$

$$\dot{\Omega}_3 = \frac{1}{I_{b_3} + J_f^{\Omega_3}} [(I_{b_1} - I_{b_2} + J_f^{\Omega_1} - J_f^{\Omega_2})\Omega_1\Omega_2 + (M_f^{v_1} - M_f^{v_2})v_1v_2 + D_{\Omega}(\Omega_3) + \rho g \mathcal{V}(-x_B \cos \theta \sin \phi - y_B \sin \theta) + \tau_{\Omega_3}] \quad (16)$$

where $G = mg - \rho g \mathcal{V}$, $m_i = m + M_f^{v_i}$, $D_v(v_i) = D_v^{i1}v_i^3 + D_v^{i2}v_i$ and $D_{\Omega}(\Omega_i) = D_{\Omega}^{i1}\Omega_i^3 + D_{\Omega}^{i2}\Omega_i$. $\varphi_v = (\varphi_{v_1}, \varphi_{v_2}, \varphi_{v_3})$ and $\tau_{\Omega} = (\tau_{\Omega_1}, \tau_{\Omega_2}, \tau_{\Omega_3})$ represent the control.

The test-bed AUV which we use for our experiments is the Omni-Directional Intelligent Navigator (ODIN), Fig.1. ODIN is owned and operated by the Autonomous Systems Laboratory (ASL), College of Engineering at the University of Hawaii (UH). The experiments are carried out at the Duke Kahanamoku Swimming Complex at UH.

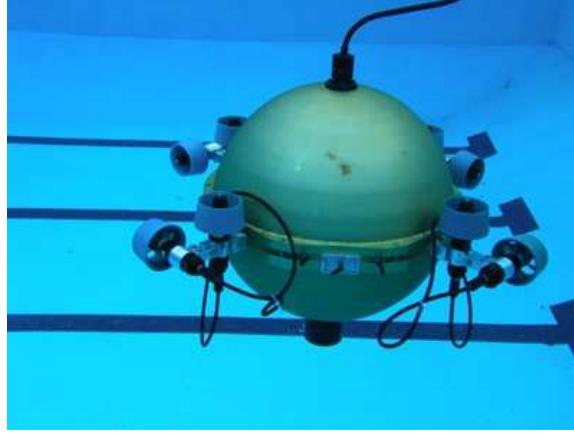


Fig.1: ODIN operating in the pool.

ODIN has a spherical hull which is 65cm in diameter. This sphere is constructed from an aluminum alloy to prevent corrosion. Eight thrusters are attached to the sphere via four fabricated mounts, each holding two thrusters. The thrusters are evenly distributed around the sphere with four vertical and four horizontal. ODIN is capable of moving in 6 degrees-of-freedom (DOF) from either a remote or autonomous mode. For our experiments, ODIN is tethered, but only to send commands via TCP/IP protocol from a shore based laptop to be run in an autonomous mode. This setup allows for multiple tests to be conducted without removing ODIN from the water to upload mission sorties. ODIN's internal CPU is a 800 MHz Intel based processor running on a PC104+ form factor with two external I/O boards providing A/D and D/A operations. Major internal components include a pressure sensor, internal navigation sensor and 24 batteries. ODIN is capable to compute real time, yaw, pitch, tilt, and depth and can run autonomously for up to 5 hours. However the yaw sensor is not designed to follow fast changes of heading ($\geq 6^\circ/s$). ODIN does not currently have real time sensors to detect horizontal (x, y) position. Instead, experiments are video taped from the 10m diving platform, giving us a near nadir view of ODIN's movements. Videos are saved and horizontal position is post processed for later analysis. A real time system utilizing sonar was available on ODIN, but was abandoned for two main reasons. First, the sonar created too much noise in the diving well and led to inaccuracies. More significantly, in the implementation of our optimal trajectories, ODIN is often required to achieve large ($> 15^\circ$) list angles which render the sonars useless for horizontal position. Many solutions were attempted and video led to the most accurate results.

The numerical values of the various parameters used for the model are given in Table I. These values were derived from experiments performed on ODIN. The added mass and drag terms were estimated from formulas found in *Allmendinger (1990)* and *Imlay (1961)*. Moments of inertia were calculated using experiments outlined in *Bhattacharyya (1978)*. We used inclining experiments to locate and place C_B in the location seen in Table I. The drag and C_B estimates were then adapted to match the experimental behavior of the vehicle.

Unique to ODIN's construction is the control from an eight dimensional thrust to move in six DOF. This construction puts redundancy into the system in case of thruster failure. ODIN is able to operate in an

under-actuated condition if necessary, and research is active in this area as well, *Catone et al. (2007)*. It is important to distinguish between the control for the real vehicle, namely the applied control referring to the action of the eight thrusters, and the six DOF introduced before in the equations of motion (4). Our input trajectories to ODIN take the form of the six DOF controls which are converted onboard ODIN to the eight dimensional actual thrusters using the following Thrust Control Matrices (TCM's):

$$TCM_{horizontal} = \begin{pmatrix} -0.707 & 0.707 & 0.707 & -0.707 \\ 0.707 & 0.707 & -0.707 & -0.707 \\ 0.48160 & -0.48160 & 0.48160 & -0.48160 \end{pmatrix}, \quad (17)$$

$$TCM_{vertical} = \begin{pmatrix} -1.0 & -1.0 & -1.0 & -1.0 \\ -0.26989 & -0.26989 & 0.26989 & 0.26989 \\ 0.26989 & -0.26989 & -0.26989 & 0.26989 \end{pmatrix}. \quad (18)$$

Table I: Numerical values for hydrodynamic coefficients.

m	126.55 kg	$\rho g \nabla$	1243.19 N	C_B	(0.49, 0.34, -7) mm
M_f^u	70 kg	M_f^v	70 kg	M_f^w	70 kg
I_x	5.46 kg.m ²	I_y	5.29 kg.m ²	I_z	5.72 kg.m ²
J_f^p	0 kg.m ²	J_f^q	0 kg.m ²	J_f^r	0 kg.m ²
D_v^{11}	-27.0273	D_v^{21}	-27.0273	D_v^{31}	-27.0273
D_v^{12}	-897.6553	D_v^{22}	-897.6553	D_v^{32}	-897.6553
D_Ω^{11}	-13.793	D_Ω^{21}	-13.793	D_Ω^{31}	-11.9424
D_Ω^{12}	-6.4594	D_Ω^{22}	-6.4594	D_Ω^{32}	-6.9393

Matrices (17) and (18) are based on the following assumptions. Let us denote by γ_i^h , $i = 1, \dots, 4$ the thrusts induced by the horizontal thrusters and γ_i^v , $i = 1, \dots, 4$ the thrusts induced by the vertical thrusters. We assume that the points of application of the thrusts $\gamma_i^{(h,v)}$ lie in a plane through the center of the vehicle. We also assume that the distance from the center of the body frame (C_G in our case) to the center of the sphere (C_B in our case) is small with respect to the radius of the sphere. As a consequence we can decouple the action of the thrusters as follows. The horizontal thrusters contribute only to the forces φ_{v_1} (surge) and φ_{v_2} (sway) and to the torque τ_{Ω_3} (yaw). The vertical thrusters contribute only to the force φ_{Ω_3} (heave) and to the torques τ_{v_1} (roll) and τ_{v_2} (pitch). We have $(\varphi_1, \varphi_2, \tau_3)^t = TCM_{horizontal}(\gamma^h)^t$ and $(\varphi_3, \tau_1, \tau_2)^t = TCM_{vertical}(\gamma^v)^t$. Assuming that the thrusters are independently powered, we can reasonably state that each thrust $\gamma_i^{(h,v)}$ is bounded by fixed values $\gamma^{(h,v)} \in \Upsilon = \{\gamma \in \mathbb{R}^8 | \gamma_i^{(h,v), \min} \leq \gamma_i^{(h,v)} \leq \gamma_i^{(h,v), \max}, i = 1, \dots, 4\}$. The image of Υ through the above linear transformation is composed of two flat ellipsoids. We choose a box included in these ellipsoids as the domain of control for the six DOF control. There are different possible choices for this box depending on the controllability properties we prefer for our vehicle. In the sequel, we assume the control domain for the component φ_v and τ_Ω to be

$$\begin{aligned} \mathcal{F} &= \{\varphi_v \in \mathbb{R}^3 | \alpha_{v_i}^{\min} \leq \varphi_{v_i} \leq \alpha_{v_i}^{\max}, \alpha_{v_i}^{\min} < 0 < \alpha_{v_i}^{\max}, i = 1, 2, 3\} \\ \mathcal{T} &= \{\tau_\Omega \in \mathbb{R}^3 | \alpha_{\Omega_i}^{\min} \leq \tau_{\Omega_i} \leq \alpha_{\Omega_i}^{\max}, \alpha_{\Omega_i}^{\min} < 0 < \alpha_{\Omega_i}^{\max}, i = 1, 2, 3\} \end{aligned} \quad (19)$$

For our numerical computations, we will take $\alpha_{v_{1,2}}^{\max} = -\alpha_{v_{1,2}}^{\min} = 8$ N, $\alpha_{v_3}^{\max} = 30$ N, $\alpha_{v_3}^{\min} = -5$ N, $\alpha_{\Omega_{1,2}}^{\max} = -\alpha_{\Omega_{1,2}}^{\min} = 3$ N.m and $\alpha_{\Omega_3}^{\max} = -\alpha_{\Omega_3}^{\min} = 1$ N.m. The non symmetry of $\alpha_{v_3}^{\min, \max}$ is due to the fact that the 4 vertical thrusters are all oriented in the same direction which is shown by the 4 negative coefficients in the first row of the matrix (18). Along with the tests to determine the values in Table I, we also tested the thrusters. Each thruster has a unique voltage input to power output relationship. This relationship is highly nonlinear and is approximated using a piecewise linear function which we refer to as our thruster model.

3 Maximum Principle

The maximum principle is a powerful tool of optimal control theory. It was developed in the 1950's and the reader can consult *Pontryagin et al. (1962)* for the original publication of this result. This principle provides necessary conditions for a trajectory to be optimal with respect to a given cost. In this section we state the maximum principle in general. The goal of this paper is not to conduct a theoretical analysis based on the maximum principle, see *Chyba et al. (2007)* for such an approach. Our goal here is to introduce the terminology to describe the trajectories that we will consider for our motion planning problem, namely the notion of bang-bang and singular arcs.

First, we rewrite the equations of motion for the submerged rigid body as an affine control system. Indeed, it is true in general that a forced affine-connection control system on a manifold Q is equivalent to an affine control system on TQ . The equivalence is realized via the *geodesic spray* of an affine-connection and the *vertical lift* of tangent vectors to Q . We introduce $\chi = (\eta, v, \Omega)$, and let $\chi_0 = \chi(0)$ and $\chi_T = \chi(T)$ be the initial and final states for our submerged rigid body. We denote the control $\varphi = (\varphi_v, \tau_\Omega)$. Thus, $\varphi_4 = \tau_1$. Then, Equation (2) is equivalent to the following affine control system:

$$\dot{\chi}(t) = Y_0(\chi(t)) + \sum_{i=1}^6 Y_i(t)\varphi_i(t) \quad (20)$$

where the drift Y_0 accounts for the centripetal, Coriolis, Drag and restoring forces. The input vector fields are given by $Y_i = (0, 0, \mathbb{I}_i^{-1})^t$ with \mathbb{I}_i^{-1} being the column i of the matrix $\mathbb{I}^{-1} = \begin{pmatrix} M^{-1} & 0 \\ 0 & J^{-1} \end{pmatrix}$. In other words, we have that $Y_i = \text{vlft}(\mathbb{I}_i^{-1})$. *Bullo and Lewis (2004)* show that trajectories for the affine-connection control system on Q map bijectively to trajectories for the affine control system on TQ whose initial points lie on the zero-section.

Let us now assume that we want to minimize a cost determined by the following expression: $C = \int_0^T f^0(\chi(t), \varphi(t))dt$. This cost can represent the time or energy consumption.

Assume that there exists an admissible cost-optimal control $\varphi = (\varphi_v, \tau_\Omega) : [0, T] \rightarrow \mathcal{U} = \mathcal{F} \times \mathcal{T}$, such that the corresponding trajectory $\chi = (\eta, v, \Omega)$ is a solution of (20) and steers the body from χ_0 to χ_T . The Maximum Principle implies that there exists an absolutely continuous vector $\lambda = (\lambda_\eta, \lambda_v, \lambda_\Omega) : [0, T] \rightarrow \mathbb{R}^{12}$, and $\lambda_0 \in \mathbb{R}$, $(\lambda_0, \lambda(t)) \neq 0$ for all t , such that the following conditions hold almost everywhere:

$$\dot{\eta} = \frac{\partial H}{\partial \lambda_\eta}, \dot{v} = \frac{\partial H}{\partial \lambda_v}, \dot{\Omega} = \frac{\partial H}{\partial \lambda_\Omega}, \quad \lambda_\eta = -\frac{\partial H}{\partial \eta}, \lambda_v = -\frac{\partial H}{\partial v}, \lambda_\Omega = -\frac{\partial H}{\partial \Omega} \quad (21)$$

where the Hamiltonian function H is given by:

$$H(\chi, \lambda, \varphi, \tau) = \lambda_\eta^t (Rv, \Theta\Omega)^t + \lambda_v^t M^{-1} [Mv \times \Omega + D_v(v)v + R^t \rho g^r \mathcal{V}k + \varphi_v] + \lambda_\Omega^t J^{-1} [J\Omega \times \Omega + Mv \times v + D_\Omega(\Omega)\Omega - r_B \times R^t \rho g^r \mathcal{V}k + \tau_\Omega] + \lambda_0 f^0(\chi, \varphi) \quad (22)$$

Furthermore, the maximum condition holds: $H(\chi(t), \lambda(t), \varphi_v(t), \tau_\Omega(t)) = \max_\gamma H(\chi(t), \lambda(t), \gamma_1, \gamma_2)$. The maximum of the Hamiltonian is constant along the solutions of (21). A quadruple $(\chi, \lambda, \varphi_v, \tau_\Omega)$ that satisfies the Maximum Principle is called an extremal, and the vector function $\lambda(\cdot)$ is called the adjoint vector.

4 Minimum Time

4.1 Singular and bang-bang arcs

In this case we have $f^0(\chi, \varphi) = 1$. The maximum condition, along with the control domain $\mathcal{F} \times \mathcal{T}$, is equivalent almost everywhere to $(M, J$ diagonal and $> 0)$, $i = 1, 2, 3$:

$$\varphi_{v_i}(t) = \alpha_{v_i}^{\min} \text{ if } \lambda_{v_i}(t) < 0 \text{ and } \varphi_{v_i}(t) = \alpha_{v_i}^{\max} \text{ if } \lambda_{v_i}(t) > 0 \quad (23)$$

$$\tau_{\Omega_i}(t) = \alpha_{\Omega_i}^{\min} \text{ if } \lambda_{\Omega_i}(t) < 0 \text{ and } \tau_{\Omega_i}(t) = \alpha_{\Omega_i}^{\max} \text{ if } \lambda_{\Omega_i}(t) > 0 \quad (24)$$

Clearly, the zeros of the functions λ_{v_i} , λ_{Ω_i} determine the structure of the solutions to the Maximum Principle, and hence of the time-optimal control. We say that a component of the control is bang-bang on a given interval $[t_1, t_2]$ if its corresponding switching functions are nonzero for almost all $t \in [t_1, t_2]$. The bang-bang component of the control only takes values in $\{\alpha_i^{\min}, \alpha_i^{\max}\}$ for almost every $t \in [t_1, t_2]$, $i = 1, \dots, 6$. On the other hand, if there is a nontrivial interval $[t_1, t_2]$ such that a switching function is identically zero, the corresponding component of the control is said to be singular on $[t_1, t_2]$. A singular control is said to be strict if all other controls are bang. We consider two types of switching times in this paper. First, assume a given component of the control to be piecewise constant, in particular this is the case if the component is bang-bang. Then, we say that $t_s \in [t_1, t_2]$ is a switching time for this component if, for each interval of the form $]t_s - \varepsilon, t_s + \varepsilon[\cap [t_1, t_2]$, $\varepsilon > 0$, the component is not constant. Secondly, a time t_s will also be referred to a switching time for a given component if it corresponds to a concatenation between a singular and a bang-bang arc for this component. In addition, when computing the total number of switching times along a trajectory we count only one switching time in the case that several components of the control switch simultaneously.

As a final remark, we would like to point out that indirect methods are numerical methods based on the Maximum Principle. The strategy is to rewrite the optimal control problem into a two point boundary value problem with the differential system being the Hamiltonian. These methods, called shooting methods, are very accurate when they converge, however in our case it would be very hard to achieve the convergence due to the bang-singular structure of the time optimal strategies in the case of the AUV's. This is why we base our strategy on direct methods as explained in the next section.

4.2 Numerical computation

A direct method is used for our numerical computations. It is based on the rewriting of the optimal control problem (*OCP*) into a finite dimensional nonlinear optimization problem (*NLOP*). The variables of the (*NLOP*) are the discretized state and control of the (*OCP*). The constraints of this (*NLOP*) are the dynamic constraints; the upper and lower bounds on the control and the final state constraint.

Methods to solve nonlinear optimization problems are well developed and we choose to use the interior point IpOpt, *Wachter and Biegler (2006)*, in conjunction with the modeling Language AMPL, *Fourer et al. (1993)*.

Due to our experimental setting we choose the initial configuration η_0 to be the origin and the final configuration $\eta_f = (5, 4, 1, 0, 0, 0)$, both at zero velocity. The limitation on the size of the trajectory is bounded by the size of the field of vision of the camera shooting the experiments ($\sim 5\text{m}$ by 7m).

There exists a trajectory between every pair of configurations at rest. Indeed, by only considering pure motions along or about one body fixed-frame axis at the time, we can realize such a trajectory with at most 6 pure motions. For our pair of configurations we need a pure surge, a pure sway and a pure heave. If we saturate the corresponding translational controls the total duration of the trajectory is $t_{\text{pure}} \approx 72.77\text{ s}$.

Numerically solving the minimum time problem for our pair of configurations provides a trajectory with a final time $t_{\text{NLOP}}^f \approx 23.21\text{ s}$. It is less than half the time for the pure motion strategy. Fig.2 shows the minimum time control strategy and trajectory.

The minimum time strategy displays a large number of switchings. We also have a singular arc for the τ_{Ω_3} control (yaw component). This singular arc emphasizes the need for the AUV to maintain a prescribed orientation in order to maximize translational controls. Such a trajectory is attractive because it is time optimal, however its implementation on a real vehicle is impossible. Indeed, close switching times are potentially damaging to the thrusters, and in fact, thrusters are physically unable to adjust to rapid switches. An additional concern is the singular arc. A control strategy that is continuously changing requires a great amount of data to be stored in the AUV's memory. Numerically, (*NLOP*) is time consuming since we need a fine discretization due to the singular arcs. Since the finer the discretization, the larger the problem, we very rapidly encounter problems with tens of thousands of variables (12 states and 6 controls per discretization step).

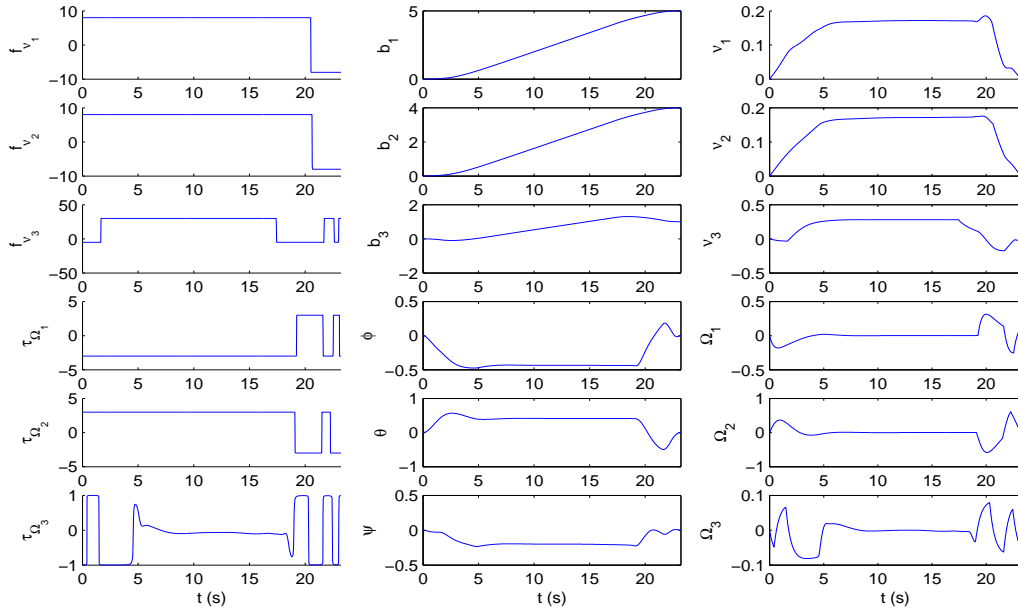


Fig.2: Minimum time trajectory, $\eta_f = (5, 4, 1, 0, 0, 0)$.

Practical considerations show the need for a trajectory to be both time efficient and implementable. A compromise between pure motions trajectories and time optimal trajectories is our goal.

First we consider a translational displacement. We can realize trajectory designs which are time efficient and implementable by considering motions with piecewise constant controls containing only one common switching time. If there are no angular velocities, then the evolutions of v_1 , v_2 and v_3 are completely decoupled. Then, given two configurations, a switching time and final time, one can always find six values of control (two values per translational control) that realize the translational motion. Of course these values of control might be out of the bounds of the thrusters. This is simply solved by increasing the switching time and the final time. Note that this is also true if there are initial or/and final translational velocities, provided they are reachable with the allocated control bounds.

Next, we extend this construction to all dimensions of the configuration space (namely the orientations), except we may be required to use more than one common switching time. Applying this idea we can choose to discretize our *(OCP)*, but only with a restricted number of discretization points; typically not more than 10, versus the 1000 plus for *(NLOP)*. The difference between this rewriting and the previous is that we take the values of the constant control and the switching times as the unknowns of the optimization problem. The new optimization problem, called the Switching Time Parameterization Problem *(STPP)_p* takes the following form:

$$(STPP)_p \begin{cases} \min_{z \in \mathcal{D}} t_{p+1} \\ t_0 = 0 \\ t_{i+1} = t_i + \xi_i, \quad i = 1, \dots, p \\ \chi_{i+1} = \chi_i + \int_{t_i}^{t_{i+1}} \dot{\chi}(t, \varphi_i, \tau_i) dt \\ \chi_{p+1} = \chi_f \\ z = (\xi_1, \dots, \xi_{p+1}, \varphi_1, \tau_1, \dots, \varphi_{p+1}, \tau_{p+1}) \\ \mathcal{D} = \mathbb{R}_+^{(p+1)} \times \mathcal{U}^{(p+1)} \end{cases} \quad (25)$$

An interesting feature of STPP is that with the low number of switching times p , it is possible to use a high order integrator to compute the dynamic constraint. This leads to a very accurate solution with respect

to the theoretical model. For practical purposes we also smooth the switchings with linear functions so they do not occur instantaneously.

Applying the nonlinear solver IpOpt to $(STPP)_p$, we get final times that are surprisingly close to the computed minimum time as shown in Table II. The first column corresponds to a given final configuration (at rest), the second to the minimum time, the third to the pure motion time, the third, fourth and fifth to $(STPP)_p$ times with 1, 2 and 5 switchings respectively. Note that the $(STPP)_p$ solutions all contain linear junctions, 120 *ms* wide, between 2 constant thrust arcs. For all these motions we take the initial configuration to be the origin.

Table II: Comparison between minimum time, pure motion time and selected $(STPP)_p$ times.

η_f	$t_{(NLOP)}^f$ (s)	t_{pure}^f (s)	$t_{(STPP)_1}^f$ (s)	$t_{(STPP)_2}^f$ (s)	$t_{(STPP)_5}^f$ (s)
(5, 4, 1, 0, 0, 0)	23.21	72.77	35.90	25.29	23.93
(5, 3, 0, 0, 0, 0)	23.04	59.18	35.90	28.89	24.46
(5, 0, 0, 0, 0, 0)	21.36	35.84	35.90	26.83	22.60
(2, 1, 0, 0.2, 0.2, 0)	11.77	30.75	16.40	14.46	12.94
(3, 4, 0, 0, 0.2, 1)	20.93	66.91	31.86	24.64	21.87

From Table II we note that the final times of the $(STPP)_p$ method are close to the minimum time even for $p = 1$, especially if we take the pure motion time as a comparison. We should note that if $(NLOP)$ and $(STPP)_p$ have the same number of discretization steps, then $(STPP)_p$ yields a shorter time because its set of admissible control strategies contain the set of $(NLOP)$ (by the variable ξ_i). Thus we clearly have the following inequalities:

$$t_{\min}^f \leq t_{(STPP)_{p+1}}^f \leq t_{(STPP)_p}^f \leq t_{(NLOP)_p}^f \quad (26)$$

Note that the first three entries for $(STPP)_1$ are the same which is not surprising since $(STPP)_1$ will give the smallest switching and final times for which the *straight line* control strategy (without change of orientation) is feasible while keeping the controls within the bounds of the thrusters. And, those times are limited here by the largest of the surge, sway and heave displacements.

Another advantage of STPP is that it is computationally efficient since the number of variables of $(STPP)_p$ is $7(p + 1)$; this is less than 50 for $p = 5$. In the cases in which it converges, $(STPP)_p$ is computationally much faster than $(NLOP)$.

Fig.3 shows the trajectory for $(STPP)_2$ with final position $\eta_f = (5, 4, 1, 0, 0, 0)$. Here the control strategy is easier to implement on a real vehicle than the time minimum strategy shown in Fig.2. The difference between the time optimal strategy and the STPP one is the fewer changes in the orientation along the $STPP$ strategy. This is directly due to the low number of switchings. Also note that the surge and sway control contain one switching time and that the important gain of time realized when adding a second switching time is due to the possibility of changing the orientation during the transfer, which is impossible when only one switching time is allowed.

For ODIN, a change of control implies a control change for at least 4 thrusters, which means a single switching strategy is easier to implement than the pure motion strategy. This is only true when considering the number of switchings of the actual thrusters, but is false if we consider that a pure motion implementation can be complemented with a feedback stabilization.

If we consider the $(STPP)$ method for the control $\gamma \in \Upsilon \subset \mathbb{R}^8$ rather than $(\varphi, \tau) \in \mathcal{F} \times \mathcal{T} \subset \mathbb{R}^6$, we are still able to compute time efficient trajectories. Fig.4 shows a $(STPP)_2$ control strategy on the control domain Υ . The minimum time for this case is $t_{(STPP)_2, \Upsilon}^f \approx 19.69$ s. Note that this is faster than the time computed for the $(NLOP)$. This is due to the transformation of Υ through the Thruster Control Matrix (17-18). This transformation forces a restriction of $\mathcal{F} \times \mathcal{T}$ to a smaller control domain than allowed by the eight dimensional control. In order to compare this with Fig.3, we also display the control strategy

given by (φ, τ) . The $(STPP)_2$ trajectory is faster since the bounds on the thrusters are loosened, thus, the switchings are of greater magnitude. There is no yaw control (τ_{Ω_3}) applied along this trajectory since all the horizontal thrust is used for φ_{v_1} and φ_{v_2} . Despite the implementability of this trajectory, the unique and unbalanced thruster behavior in conjunction with the larger magnitude thrusts exaggerates errors here more than in the six dimensional $(STPP)$ strategy. Thus, we restrict ourselves to the control domain $\mathcal{F} \times \mathcal{T}$ to minimize the effect of the thrusters' dynamic differences, over which we have no control.

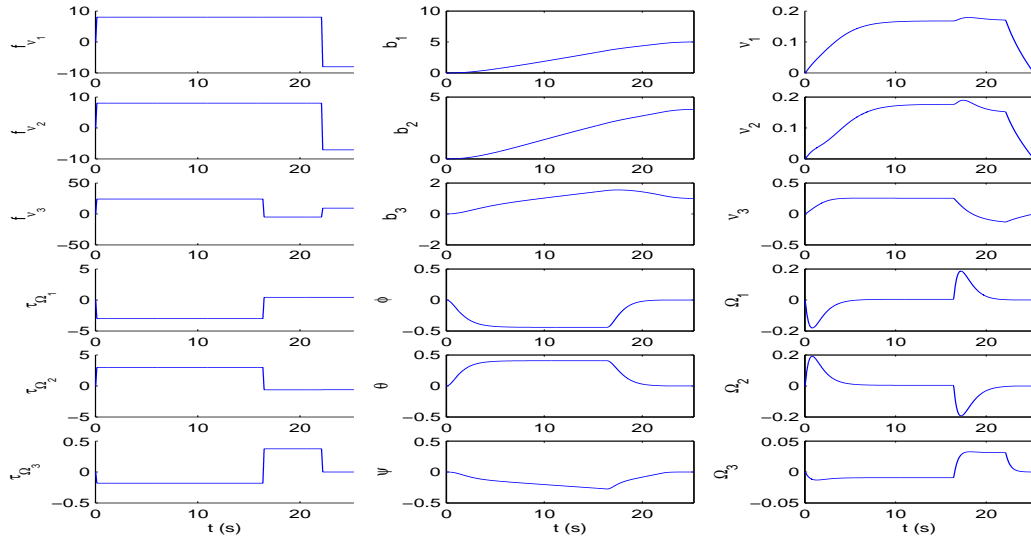


Fig.3: $(STPP)_2$ trajectory for $\eta_f = (5, 4, 1, 0, 0, 0)$.

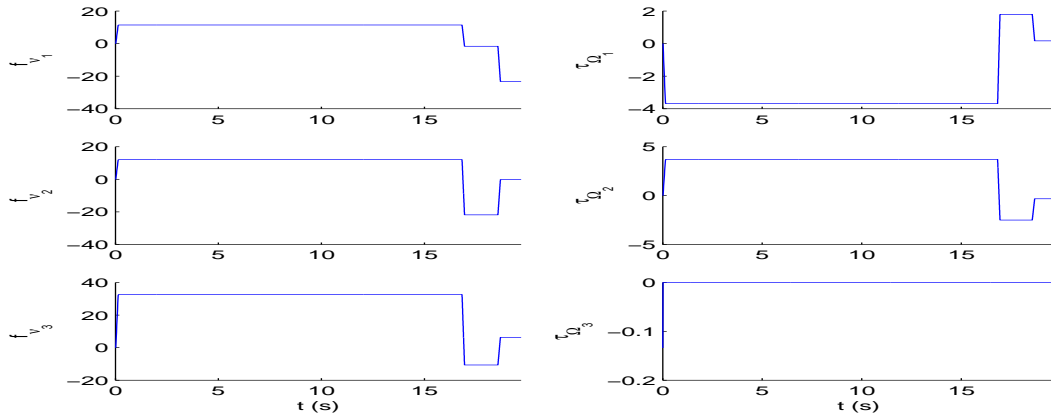


Fig.4: $(STPP)_2$ trajectory for $\eta_f = (5, 4, 1, 0, 0, 0)$ and control domain Υ .

4.3 Experiments

Fig.5 shows the result of the implementation of a pure motion trajectory onto ODIN. The pure motion open loop control in surge, sway and heave is complemented with a feedback control on pitch, roll and yaw. This feedback on orientation compensates for the physical unbalancing of the thrusters. We represent the surge and sway evolution in the picture. The solid line is the actual trajectory realized by

ODIN. The dotted line represents the trajectory obtained using our theoretical model with the thrusts actually applied to ODIN during the test. In the theoretical model, we impose the yaw evolution to be that of experiment, otherwise the horizontal direction diverges very fast due to the sensitivity of the yaw (no restoring moment in yaw).

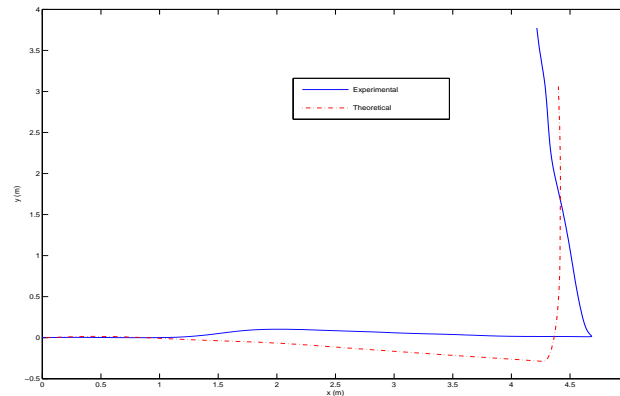


Fig.5: Comparison between the pure motion experimental surge, sway evolution and the theoretical evolution (with yaw correction) $\eta_f = (5, 4, 1, 0, 0, 0)$.

Fig.5 validates our theoretical model. Despite many challenges in experimentation at the pool, we observed excellent behavior by ODIN. The difference in heading is the result of our inertial measurement unit's sensitivity to the surrounding magnetic field generated by pool's metal wall and the recirculation pumps. The small difference in surge and sway magnitude are due to factors such as underestimation of damping, imperfection in thruster modeling, pool current and the drag induced by the umbilical tether. The drag from the tether greatly depends on the tether location at the beginning of an experiment. This drag is difficult to take into account due to its variance. The current in the pool is dependent on location and is currently under investigation.

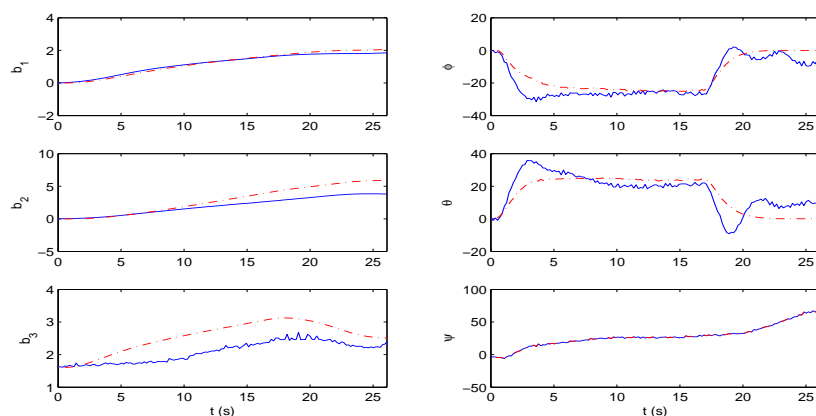


Fig.6: Comparison between $(STPP)_2$ experimental (plain) and theoretical (dashed) trajectories for $\eta_f = (5, 4, 1, 0, 0, 0)$.

Fig.6 shows the experimental evolution of the implementation of the $(STPP)_2$ control strategy of Fig.3. For comparison, we display the theoretical behavior of the AUV for which the yaw evolution has been corrected similarly to the pure motion analysis. Note that in this experiment, we do not use any feedback

control. We obtained a very good response from ODIN. Its trajectory closely follows the theoretical one. However, we see the heave evolution is not reliable which comes from the drag and slight positive buoyancy of the tether. ODIN is only positively buoyant by only 3 N, thus any change in buoyancy will have a noticeable impact on the depth evolution. The surge and sway are also influenced by the drag of the tether and pool current which explains the theoretical over estimation of their evolutions. We see an overshooting in the pitch and roll experimental evolution. This is partially due to the un-modeled transient behavior of the thrusters.

5 Minimum Energy Consumption

5.1 Criterion

Since we are able to design practical time efficient trajectories, we now consider an energy criterion. Such a criterion is directly related to the physical model considered. Since AUV's are powered by internal batteries, we consider maximization of the life span of the batteries. The majority of the energy consumption of an AUV is the thrusters, while the on-board computer and sensors only play a marginal role. For ODIN, the thrusters are powered by a constant 24 V. We represent the consumption of one thruster by the current it pulls. Since the life span of a battery is given in Amps.hour, the criterion to consider for one thruster is the integral of the pulled current over the trajectory duration. Since ODIN has eight thrusters, the criterion will have the form

$$J = \min \sum_{i=1}^8 \int_0^{t^f} I(\gamma_i(t)) dt \quad (27)$$

where $\gamma_i(t)$ represents the thrust delivered by the i^{th} thruster and $I(\cdot)$ is a function which gives the pulled current with respect to a given thrust. Note that $I(\cdot)$ may be unique for each thruster. For simplicity, we do not consider such a refinement and assume $I(\cdot)$ equal for all thrusters.

For the criterion J , we have three choices for the final time; we fix it, we introduce it into the criterion as a weighted final time to minimize, or we leave it free. Since our mechanical system is dissipative, the third choice will still yield a finite final time. Also, there exists a finite final time with minimum energy consumption such any increase in time uses more energy to compensate the dissipative forces without gaining efficiency over the trajectory. Let us denote by t_{\min}^J the final time which yields the minimum consumption. Then any solution of the fixed final time minimum energy consumption with $t^f < t_{\min}^J$ will be a solution of the weighted minimum consumption and minimum time (the second choice) for a specific choice of weights.

We fix t^f as a multiple of the minimum time computed using the methods of Section 4: $t^f = c_{t^f} t_{\min}^J$ and $c_{t^f} > 1$. This problem does not have a solution for $c_{t^f} < 1$ and the solution for $c_{t^f} = 1$ is the minimum time solution.

Since criterion (27) explicitly involves the eight thrusters, the proper domain of controllability is the complete eight dimensional domain Υ . Indeed, if we insist on using the simplified six dimensional control φ and τ we will encounter an intricate criterion. Hence, we use the eight dimensional control γ , remembering that φ and τ are obtained from γ through the linear transformations (17-18).

Computing the (OCP) associated to (27) depends on the function $I(\cdot)$. From experimental measurements, we conclude that an accurate approximation of $I(\cdot)$ is a piecewise linear function:

$$I(\gamma) = \begin{cases} -0.192\gamma & = \alpha\gamma, \text{ if } \gamma \leq 0 \\ 0.408\gamma & = \beta\gamma, \text{ if } \gamma \geq 0 \end{cases} \quad (28)$$

Notice that C^2 -functions are usually required for a numerical optimizer to converge. Moreover, our criterion is non differentiable at the minimum of the pulled current. This is a critical point which plays an important role in minimization. Applying the maximum principle to J gives a control strategy of bang-bang controls connected by singular arcs. Thus, we first smooth J . For this, we consider two fourth order

polynomials P_α, P_β (covering the negative and positive γ respectively). These polynomials form a C^2 -junction P_α/P_β at zero, I/P_α at a negative thrust (γ_α) and P_β/I at a positive thrust (γ_β). Let $\varepsilon > 0$ and $P_\alpha(0) = P_\beta(0) = \varepsilon$. This gives $P_\alpha(\gamma) = \alpha_4\gamma^4 + \alpha_3\gamma^3 + \varepsilon$ and $P_\beta(\gamma) = \beta_4\gamma^4 + \beta_3\gamma^3 + \varepsilon$ where

$$\begin{cases} \gamma_\alpha = 2\varepsilon/\alpha \\ \alpha_4 = -\alpha^4/(16\varepsilon^3) \\ \alpha_3 = \alpha^3/(4\varepsilon^2) \end{cases}, \begin{cases} \gamma_\beta = 2\varepsilon/\beta \\ \beta_4 = -\beta^4/(16\varepsilon^3) \\ \beta_3 = \beta^3/(4\varepsilon^2) \end{cases} \quad (29)$$

. We see that as ε tends to zero, I approaches the smoothed function. Let us call our smoothed current/force function I_ε and the corresponding smoothed criterion J_ε . Before attempting a numerical solution, we take a look at the extremal of the problem, as given by the Maximum Principle.

5.2 Extremal of Consumption

From the maximum principle, the structure of the eight dimensional extremal control is given by eight functions κ_i , $i = 1, \dots, 8$. These functions are a linear combination of the co-adjoint variables λ_{v_i, Ω_i} with linear coefficients coming from the Thruster Control Matrix (17-18). For example, the function κ_1 , describing the control γ_1 , is given by: $\kappa_1 = -\frac{\sqrt{2}\lambda_{v_1}}{2(m+M_f^{v_1})} + \frac{\sqrt{2}\lambda_{v_2}}{2(m+M_f^{v_2})} + \frac{0.4816\lambda_{v_3}}{I_{b_3+J_f^{v_3}}}$. Note that the κ_i would be the switching functions if we were to consider the minimum time problem with γ as control.

The maximization of the Hamiltonian is similar for all control γ_i . If we denote by $\bar{\gamma}_i$ the control that maximize the Hamiltonian we get:

$$\bar{\gamma}_i = \begin{cases} \gamma_i^{\min} & , \text{ if } \kappa_i < \alpha \\ \in [\alpha_i, \gamma_\alpha] & , \text{ if } \kappa_i = \alpha \\ \text{unique root of } \kappa_i - P'_\alpha \in [\gamma_\alpha, 0] & , \text{ if } \kappa_i \in (\alpha, 0) \\ 0 & , \text{ if } \kappa_i = 0 \\ \text{unique root of } \kappa_i - P'_\beta \in [0, \gamma_\beta] & , \text{ if } \kappa_i \in (0, \beta) \\ \gamma_i^{\max} & , \text{ if } \kappa_i > \beta \end{cases} \quad (30)$$

. From this maximization, we see that if γ_β or γ_α are within the bounds of the control, then it is possible for an extremal to have discontinuity in the control. Since the κ_i are absolutely continuous functions, two constant control phases will be linked by a continuous control. However, if c_{if} is large enough, we can always expect the control to be continuous without ever being saturated.

5.3 Numerical results

We use the direct method (*NLOP*) to gain insight to such strategies. Multiple shooting methods are currently under investigation. Fully discretizing the (*OCP*) in state and control, we can again apply the *IpOpt* solver along with the modeling language *AMPL*. Despite the problem being significantly more sensitive, we can compute optimal solutions for a various collection of c_{if} . For $\eta_f = (5, 4, 1, 0, 0, 0)$, we take $t_{\min}^f \approx 23.21$ s, the minimum time of the six dimensional controlled system. Before looking at specific control strategies, we consider the evolution of energy consumption with respect to c_{if} shown in Fig.7. In the right diagram of Fig.7, the criterion J is not minimized. So, it is not surprising to have an evolution depending on ε . As expected, J is not decreasing with c_{if} , but has a minimum for some final time $t_{\min}^{J_\varepsilon}$ which depends on ε . It is of interest to study the dependency of $t_{\min}^{J_\varepsilon}$ with respect to ε , as well as the dependency of $t_{\min}^{J_\varepsilon}$ with respect to the buoyancy of the vehicle and the position of C_B . However, we will not address these questions here.

For initial configuration at the origin and $\eta_f = (5, 4, 1, 0, 0, 0)$, there are numerous minimum consumption strategies to consider. Nevertheless, a first choice is one that approximately corresponds to $t_{\min}^{J_\varepsilon}$. Fig.8 shows the thrust evolution and trajectory corresponding to $\varepsilon = 0.5$ and $c_{if} = 2$.

In Fig.8, we display the controls φ and τ rather than γ since they are more meaningful, even though they are not used in the optimization process. Compare this trajectory to the minimum time trajectory shown

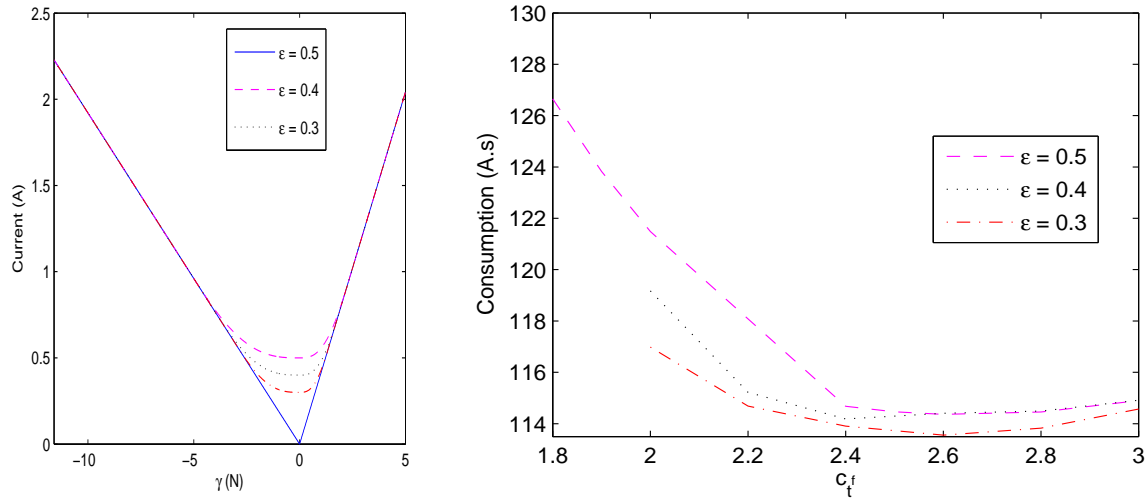


Fig.7: Smoothed function I_ϵ (left) and evolution of the consumption J w.r.t. c_{t^f} for $\eta_f = (5, 4, 1, 0, 0, 0)$ and $\epsilon = 0.5, 0.4$ or 0.3 (right)

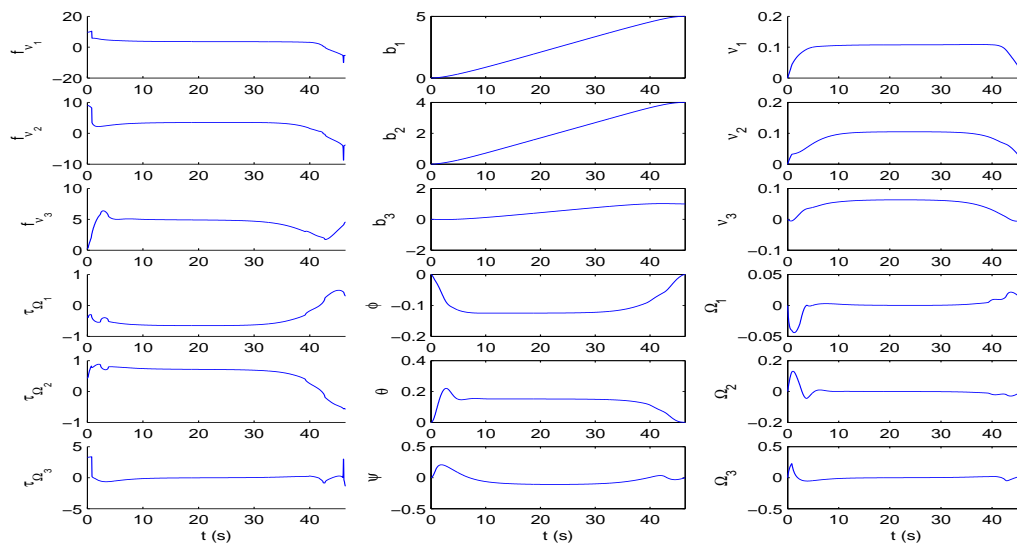


Fig.8: Minimum consumption control strategy and trajectory for $\eta_f = (5, 4, 1, 0, 0, 0)$, $t^f = 46.42$ s and $\epsilon = 0.5$.

in Fig.2. The first obvious difference is the magnitude of the control. For the minimum consumption control strategy, there is minimal actuator saturation, while for the minimum time strategy actuators are saturated for the entire motion.

As is, the minimum energy consumption strategies will be very hard to implement for two main reasons. First, the continuous evolution of the control strategy is not implementable on a real vehicle, and even a discretization would require the storage of impractical amounts of data. Secondly, considering low magnitude thrusts will exaggerate the ODIN's sensitivity to the unmodeled external forces such a tether drag and pool current. For these reasons it would be interesting to adapt the (STPP) method to the energy consumption problem and consider final times which are closer to the minimum time. This will ensure a greater thrust magnitude while still saving energy.

It is reasonable that an adaptation of (*STPP*) is feasible. Indeed extremal strategies will contain constant thrust arcs of maximum and zero magnitude by the maximum principle applied to J . These strategies, will be easier to implement than continuous evolutions provided we take precautions to smooth the transitions between thrust arcs.

Acknowledgements

Research supported by NSF grant DMS-030641 and DMS-0608583 and partially supported by ONR grant #N00014-03-1-0969, #N00014-04-1-0751 and #N00014-04-1-0751.

References

- ALLMENDINGER, E. (1990), *Submersible vehicle design*, SNAME
- BERTRAM, V.; ALVAREZ, A. (2006), *Hydrodynamic aspects of AUV design*, 5th Int. Conf. Computer Applications and Information Technology in the Maritime Industries, Leiden
- BHATTACHARYYA, R. (1978), *Dynamics of Marine Vehicles*, Wiley
- BULLO, F.; LEWIS, A.D. (2004), *Geometric Control of Mechanical Systems Modeling, Analysis, and Design for Simple Mechanical Control Systems*, Springer-Verlag, New York-Heidelberg-Berlin, 49 in Texts in Applied Mathematics
- CATONE, C.; CHYBA, M.; SMITH, R.N.; WILKENS, G.R. (2007) *Decoupling vector fields for the submerged rigid body in an ideal fluid*, Preprint
- CHYBA, M.; HABERKORN, T.; SMITH, R.N.; WILKENS, G.R. (2007), *Geometric properties of singular extremals for a submerged rigid body*, Preprint.
- FOSSEN, T.I. (1994), *Guidance and control of ocean vehicles*, Wiley, New York
- FOURER, R.; GAY, D.M.; KERNIGHAN, B.W. (1993), *AMPL: A Modeling Language for Mathematical Programming*, Duxbury Press, Brooks-Cole Publ.
- IMLAY, F.H. (1961), *The complete expressions for added mass of a rigid body moving in an ideal fluid*, Technical Report DTMB 1528
- LEONARD, N.E. (1997), *Stability of a bottom-heavy underwater vehicle*, Automatica 33/3, pp.331-346
- LEONARD, N.E. (1996), *Stabilization of Steady Motions of an Underwater Vehicle*, 35th IEEE Conf. Decision and Control
- MACIVER, M.A.; FONTAINE, E.; BURDICK, J.W. (2004), *Designing future underwater vehicles: Principles and Mechanisms of the Weakly Electric Fish*, IEEE J. Oceanic Eng. 29/3
- MOLNAR, L.; OMERDIC, E.; TOAL, D. (2005), *Hydrodynamic aspects of AUV design*, Ocean 2005 Europe IEEE Conf., Brest
- PONTRYAGIN, L.S.; BOLTYANSKI, B.; GAMKRELIDZE, R.; MICHTCHEKNO, E.(1962), *The Mathematical Theory of Optimal Processes* Interscience, New York
- WAECHTER, A.; BIEGLER, L.T. (2006), *On the implementation of an interior-point filter-line search algorithm for large-scale nonlinear programming*, Research Report RC 23149, IBM T.J. Watson Research Center, Yorktown